mater.scichina.com link.springer.com

Published online 16 May 2024 | https://doi.org/10.1007/s40843-024-2961-5
Sci China Mater 2024, 67(6): 1915–1925

Versatile graphene/polyelectrolyte aqueous dispersion for fiber-based wearable sensors and electroluminescent devices

Zhenyu Miao, Rouhui Yu, Xiaowen Bai, Xiangheng Du, Zhonghua Yang, Tao Zhou, Meifang Zhu and Shaowu Pan*

ABSTRACT **Conductive dispersion is a crucial building block for obtaining conductive fibers/textiles used in wearable sensing, energy supply, and flexible display devices. However, despite the graphene's stable chemical properties and high electrical conductivity, fabricating graphene dispersions compatible with fiber/textile materials remains challenging. Here, an eco-friendly and stable graphene aqueous dispersion was fabricated by introducing poly(sodium-p-styrenesulfonate) (PSS) dispersant based on non-covalent interactions. Due to the modification of PSS, graphene carries negative charges, and the resulting electrostatic repulsion promotes the stable dispersion of graphene. Moreover, PSS assists graphene in forming a robust adhesion to substrates. Flexible mechanical sensors using graphene-modified fibers and fibrous membranes, including stretchable strain sensors and pressure sensors, were developed, showing high stretchability of up to 100% with a sensitivity of 144.6, capable of a sensing strain as small as 0.1%. Flexible electrophysiological electrodes were also fabricated to record electromyography and electrocardiograph signals for a long time. As a proof of concept, a coaxial electroluminescent fiber was demonstrated to provide illumination for a submarine model to complete complex tasks. This advancement will further propel the advanced nanomaterials into wearable fields.**

Keywords: graphene dispersion, fibers, mechanical sensors, wearable display

INTRODUCTION

Fiber-based electronic devices, with their lightweight, flexibility, and weavability, present an ideal platform for constructing smart wearable textiles. These devices have attained various functionalities, including strain and pressure sensing, humidity and temperature monitoring, gas detection, thermoelectric conversion, energy storage, and flexible display [1–14]. It is critically important to endow polymeric fibers with electrical conductivity to develop various functions [15,16]. Solution-based processing is an effective and easy scale-up method for integrating conductive materials with fibers and textiles while maintaining structural integrity [17–19]. The primary performance factors of conductive dispersions include conductivity, stability, environmental friendliness, and compatibility with substrates. Furthermore, the biocompatibility of conductive dispersion is crucial for fiber-based flexible devices intended for wearable applications [20]. The conductive dispersions that exhibit high conductivity, excellent dispersion, and strong compatibility with fibers are highly desired.

Graphene has attracted considerable attention in flexible electronic device owing to its high conductivity, robust mechanical properties, and excellent chemical stability [21,22]. Solution processing is a critically important method for achieving a large-scale application of graphene. However, the substantial specific surface area and strong interactions between graphene sheets make them prone to aggregation. There are two typical strategies to fabricate graphene-based solution/dispersions. One method involves the chemical oxidation of graphite to produce hydrophilic graphite oxide, resulting in a stable graphene oxide solution [23–26]. However, due to its non-conductive nature, graphene oxide requires a reduction process involving chemical reagents, high-temperature treatment, ultraviolet-assisted methods, and other techniques to restore its electrical conductivity [27–31]. However, the harsh reduction conditions can damage the structure of polymer fibers and textiles, as well as other active materials in electronic devices. Another approach involves adding dispersion additives to graphene dispersions to reduce strong π-π interactions between graphene sheets, thereby forming stable graphene dispersions. To date, small molecular surfactants have been widely used to disperse graphene [32,33]. The hydrophobic carbon chains in small molecular surfactants can orderly arrange themselves on the surface of graphene *via* hydrophobic adsorption, which enhances the surface activity of graphene, thus realizing the effective dispersion of graphene [34]. However, small molecule surfactants cannot be effectively decorated on the graphene surface due to their short molecular chains, resulting in poor ability to disperse graphene, which in turn affects the conductivity of the graphene dispersion. Furthermore, small molecular surfactants typically exhibit poor adhesion to polymer substrates, such as fibers, textiles, and stretchable polymers, leading to unstable performance of flexible electronic devices. Therefore, it is necessary to develop stable conductive dispersions using water as the solvent, especially those with robust adhesion to flexible polymer substrates. Polyelectrolytes play a

State Key Laboratory for Modification of Chemical Fibers and Polymer Materials, College of Materials Science and Engineering, Donghua University, Shanghai 201620, China
* Corresponding author (email: pansw@dhu.edu.cn)

crucial role in the field of dispersion due to their ability to impart surface charge to nanomaterials [35,36]. Poly(sodium-p-styrenesulfonate) (PSS), as a typical polyelectrolyte, has hydrophobic long alkane chain and benzene ring to form hydrophobic and π-π interactions with graphene, and hydrophilic sulfonic acid groups can form hydrogen bonds with water. This effect may promote the dispersion and substrate adhesion of graphene.

In this work, we reported an easy scale-up graphene/PSS aqueous dispersion, with stable adhesion to polymer fiber substrates, and demonstrated its versatile applications in fiber-based electronic devices (Fig. 1a). The high-molecular-weight PSS could effectively disperse graphene in aqueous solution through non-covalent interactions and electrostatic repulsion, and further facilitate the integration of graphene with fibers and textiles to achieve durable conductive fibers/textiles (Fig. 1b–d). Flexible mechanical sensors, including stretchable strain sensors, pressure sensors, electrophysiological electrodes and fiber electroluminescent devices were developed based on graphene nanosheet/PSS (GNS/PSS)-decorated conductive fibers. These devices were utilized in electromyography (EMG) and electrocardiography (ECG) recording, as well as underwater illumination.

EXPERIMENTAL SECTION

Materials

Expanded graphite (EG) (325 mesh) was purchased from Suqian Xigu Nanotechnology Co., Ltd. ZnS:Cu phosphor powder was purchased from Shanghai Keyan Optoelectronics Technology Co., Ltd. A PEDOT:PSS aqueous solution (Clevios PH 1000) was purchased from Heraeus Co., Ltd. PDMS (Sylgard 184) was obtained from Dow Corning Corporation. PSS (Mw ~70,000), polyvinyl alcohol (PVA, 1788), Styrene-butadiene-styrene block copolymers (SBS), Styrene-isoprene-styrene block copolymers (SIS), dimethyl sulfoxide (DMSO), cyclohexane and ethylene glycol were obtained from Shanghai Titan Technology Co., Ltd. All other materials and reagents were commercially available and used without purification.

Preparation of GNS/PSS dispersion

Firstly, PSS was dissolved in 100 mL of deionized water at various weights (0.33, 0.67, 1.00 and 1.34 g). Then, 0.67 g of EG was added to the PSS aqueous solution. The mixture was sonicated for 2 h using a sonicator (SCIENTZ-IID, Scientz, China) under a power of 250 W. Dry GNS/PSS powder was obtained by freeze-

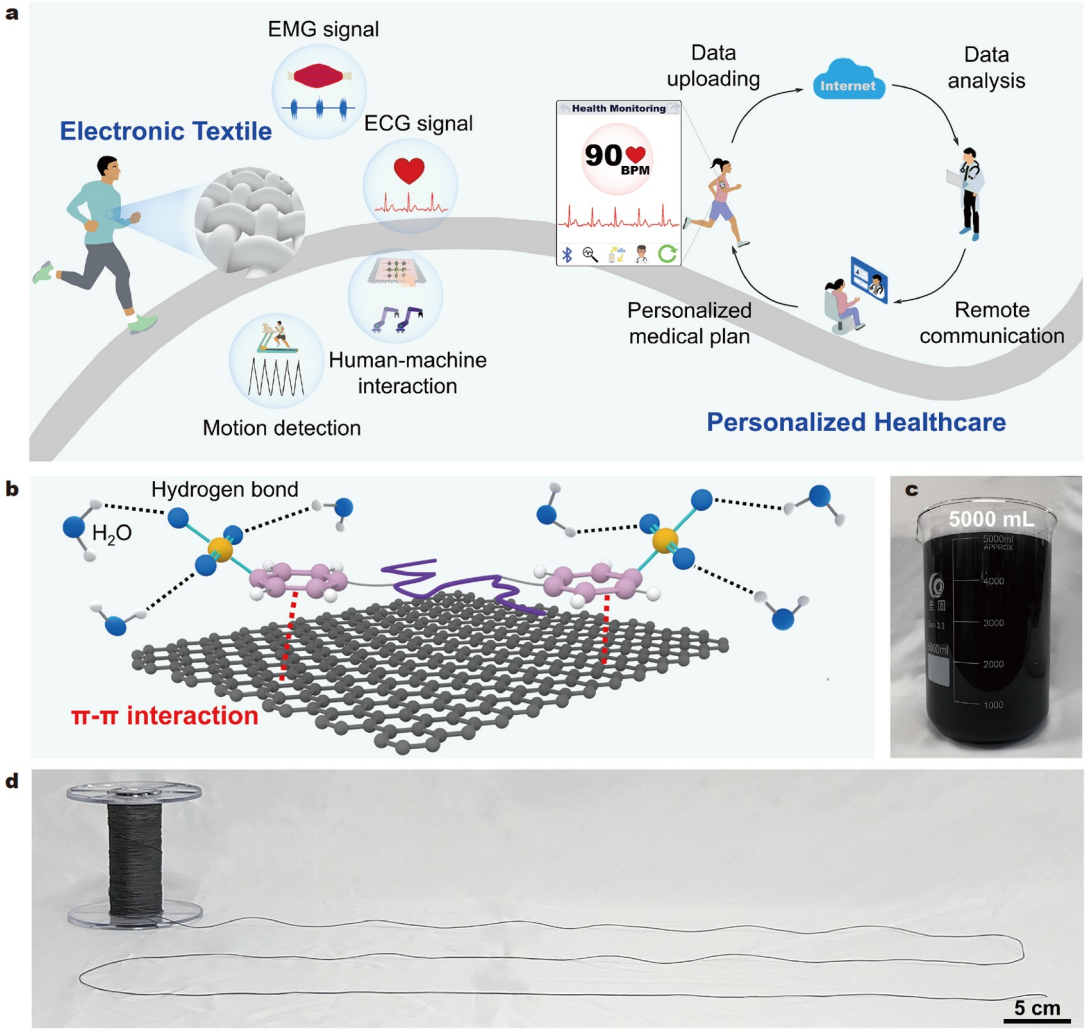

Figure 1 (a) Fiber-based electronic textiles for electrophysiological signal monitoring and wearable personalized healthcare. (b) The design of GNS/PSS aqueous dispersions based on π-π interactions. (c) A photo of a 5000-mL large-volume GNS/PSS dispersion. (d) A photo of 20-m-long conductive fiber of GNS/PSS-modified PA6.

drying GNS/PSS dispersion. Upon dispersing the GNS/PSS powder in water (with a fixed GNS content of 1.63 wt%), four kinds of GNS/PSS dispersions were obtained, named as $GNS_1/PSS_{0.5}$, GNS_1/PSS_1, $GNS_1/PSS_{1.5}$ and GNS_1/PSS_2, respectively. In a control experiment, 0.67 g of EG was added to 100 mL of deionized water for sonication under the same conditions, and the freeze-dried sonicated EG powder was also dispersed in water (sonicated EG content was 1.63 wt%) to obtain sonicated EG dispersion. Then, 0.67 g of EG was added to 0.33 g of sodium dodecyl benzene sulfonate aqueous solution (100 mL), and a dispersion of $GNS_1/SDBS_{0.5}$ was prepared under the same conditions.

Fabrication of a fiber strain sensor

The commercial Thermoplastic polyurethane (TPU) fiber, with a diameter of 500 μm, was selected as the substrate for the strain sensor due to its excellent flexibility and elasticity. Firstly, TPU fiber was pretreated in a DMSO solution for 2 s. Then, the residual DMSO on the fiber surface was rinsed off in ethanol and deionized water in turn. Finally, the treated TPU fiber was soaked in $GNS_1/PSS_{0.5}$ dispersion. GNS/PSS-decorated TPU fibers with varying conductivity were obtained after sonication for 1, 2, 3, 4, 5, 6 and 7 min with a 200-W power.

Fabrication of a nanofiber membrane-based pressure sensor

TPU particles were dissolved in the mixed solvent of DMF and THF (1:1 mass ratio) to prepare 20 wt% TPU spinning solution. The TPU nanofiber membrane was then prepared by electrospinning at a flow rate of 3 mL/h and a voltage of 15 kV. Two pieces of TPU nanofiber membranes (20 × 20 mm^2) with a thickness of 120 μm were adhered to the surface of medical adhesive tape (25 × 25 mm^2), and a conductive path (20 × 3 mm^2) was coated with $GNS_1/PSS_{0.5}$ dispersion at their central positions. After drying, copper wires were connected to one end of the conductive path with silver paste, which served as the top and bottom electrodes of the device. Secondly, a nanofiber membrane (10 × 10 mm^2) with the same thickness was soaked in the $GNS_1/PSS_{0.5}$ dispersion, and the intermediate sensing layer was obtained after being dried by sonication at 200 W for 5 min. Finally, the sensing layer was placed on the bottom electrode, the top electrode was positioned perpendicular to the bottom electrode on the sensing layer. The cross-sectional area between the electrodes was designated as the sensing area, thus forming a pressure sensor with a sandwich structure.

Fabrication of a fabric bandage electrode

Firstly, the TPU nanofiber membrane (8 × 20 mm^2) with a thickness of 120 μm was sonicated in $GNS_1/PSS_{0.5}$ dispersion at a power of 200 W for 5 min to produce a conductive nanofiber membrane. Secondly, commercial bandages were used as the fabric substrate, and the conductive nanofiber membrane was fixed on the surface of the fabric bandage that contacted the skin using copper wires. One conductive nanofiber membrane was fixed at the center of two fabric bandages to build ECG fabric bandage electrodes. Three conductive nanofiber membranes were attached to single fabric bandage with a spacing of 10 mm in order to form EMG fabric bandage electrodes.

Detection of electrophysiological signals

The HealForce ECG recorder (PC 80B) was used to record ECG signals. Two ECG fabric bandage electrodes were worn near the wrist of the forearm serving as working electrodes. A commercial gel electrode was used as the reference electrode. The ECG data were extracted using MATLAB and then redrawn by Origin. The epidermal EMG signal collector (ZJE-Ⅱ-2) was used to record EMG signals. The EMG fabric bandage electrode was worn on the flexor of writ of forearm. Copper wire was used to connect the fabric bandage electrode with the acquisition equipment for detecting electrophysiological signals.

Fabrication of a coaxial electroluminescent fiber

Firstly, a 1-meter long PA6 yarn was sonicated in $GNS_1/PSS_{0.5}$ dispersion at 200 W for 20 min to obtain conductive PA6 yarn. Subsequently, conductive PA6 yarns were used as internal electrodes and an emission layer was coated on them by spraying. The emissive layer was made of ZnS:Cu/SBS cyclohexane dispersion at the concentrations of 2 and 2.8 wt%, respectively. Then, layers of a 2 wt% PVA solution, the PEDOT:PSS/ethylene glycol aqueous solutions (at concentrations of 0.13 and 5 wt%, respectively) and PDMS prepolymer (at a ratio of 10:1) were successively coated onto the surface of the emissive layer. These layers served as hydrophilic modification layer, external electrode layer and hydrophobic encapsulation layer, respectively.

RESULTS AND DISCUSSION

The fabrication schematic of GNS/PSS dispersion was shown in Fig. S1. EG was used to fabricate GNS/PSS aqueous dispersion, and its surface morphology was shown in Fig. S2. PSS serves as both the surfactant and intercalator, facilitating the exfoliation of EG in water to yield the graphene dispersion. The sulfonic acid groups at the hydrophilic end of PSS form hydrogen bonds with water molecules, which reduce the surface tension of water and thus enhance the water wettability of graphene [37]. Subsequently, the cavitation effect during the ultrasonic process induces the formation of gaps at the edges of EG, allowing PSS to infiltrate the interlayers of graphite (Fig. S1) [38]. This infiltration increases the interlayer spacing of EG and diminishes the Van der Waals force between the layers [39]. Simultaneously, the benzene rings and long alkyl chains located at the hydrophobic end of PSS readily engage in strong π-π interactions and hydrophobic interactions with graphene, thereby enhancing the adsorption of graphene by PSS [40]. Consequently, graphene is effectively dispersed in water. We first characterized the surface morphology of PSS on the GNS surface using Scanning Electron Microscope (SEM). It is clear that the surface of the sonicated EG appears flat, whereas the surface of GNS modified by PSS displays a series of white spots (Fig. 2a, b). It is confirmed that GNS was successfully modified by PSS according to a previous work [41]. Furthermore, the edge of PSS-modified GNS was transparent from the TEM image (Fig. 2c), confirming the successful exfoliation of EG by PSS into few-layer graphene *via* non-covalent modification [42]. This successful exfoliation can also be confirmed by the specific surface area results of EG and GNS/PSS. BET results show that the specific surface area increases from 14.71 to 149.95 m^2/g when EG is exfoliated into GNS/PSS (Fig. S3).

To evaluate the impact of PSS on the stability of GNS/PSS dispersion, we studied the dynamic instability of GNS/PSS dispersion with varying PSS contents *via* multiple light scattering [43]. The dynamic instability of all GNS/PSS dispersions remained low. Particularly, the $GNS_1/PSS_{0.5}$ sample exhibited the

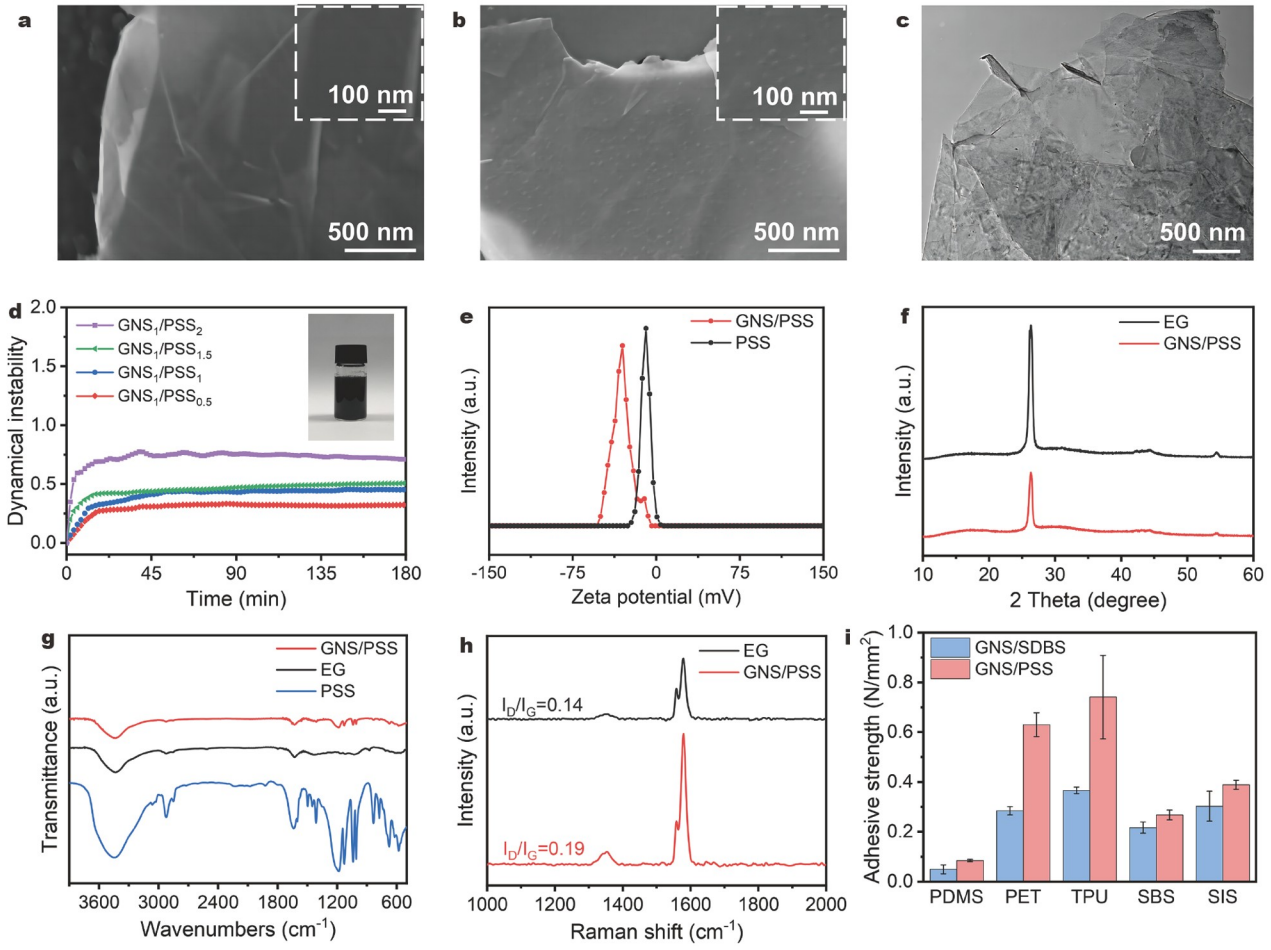

Figure 2 Characterization of the structure and properties of the GNS/PSS aqueous dispersion. SEM images of sonicated EG (a) and GNS/PSS (b); inset shows their enlarged images. (c) TEM image of GNS/PSS. (d) Dependence of the dynamical instability of GNS/PSS on the PSS loading; inset shows the optical image of $GNS_1/PSS_{0.5}$ dispersion. (e) Zeta potentials of PSS solution and $GNS_1/PSS_{0.5}$ dispersion. (f) XRD spectra of EG and $GNS_1/PSS_{0.5}$. (g) FTIR spectra of EG, $GNS_1/PSS_{0.5}$ and PSS. (h) Raman spectra of EG and $GNS_1/PSS_{0.5}$. (i) The adhesion strength of conductive materials from $GNS_1/SDBS_{0.5}$ and $GNS_1/PSS_{0.5}$ with different substrates.

lowest dynamic instability (Fig. 2d). Both sonication time and power affect the dispersion performance. As sonication time and power increase, the dynamic instability of dispersion decreases, indicating improved dispersion performance. With an ultrasonic duration of 2 h and ultrasonic power exceeding 250 W, dispersion performance reaches stability (Fig. S4). In contrast, the sample of sonicated EG precipitated within 10 min, showing high dynamic instability (Fig. S5). The results indicated that the presence of PSS significantly enhanced the stability of GNS/PSS dispersions. When dropping sonicated EG and GNS/PSS dispersions into water, the $GNS_1/PSS_{0.5}$ dispersion diffused fully in the water, while the sonicated EG dispersion immediately reaggregated upon contact with water (Fig. S6). This phenomenon convincingly demonstrated the dispersing effect of PSS on GNS. To investigate the underlying reason for the difference in dynamic instability among GNS/PSS dispersions with varying PSS contents, zeta potential was measured to analyze the surface properties of GNS/PSS nanocomposites. The zeta potential of $GNS_1/PSS_{0.5}$ dispersion and PSS solution were −30.3 and −9.2 mV, respectively (Fig. 2e). PSS shows a negative charge due to the presence of sulfonic acid groups, while GNS itself contains a small amount of oxygen-containing functional groups, resulting in a negative charge as well. Therefore, the GNS modified by PSS possesses more negative charges, enhancing electrostatic repulsion between GNS and promotes their effective dispersion in water. In addition, it is known that zeta potential decreases with increasing ion concentration in solution [44]. Therefore, the ionic concentration in the dispersion increases as the PSS content grows, resulting in the decrease in the zeta potential of the GNS/PSS dispersion. This reduction weakens the electrostatic repulsion between GNS, thus reducing the dispersion capability of GNS in water. It should be noted that increasing the PSS content inevitably decreases the conductivity of GNS/PSS (Fig. S7). Considering both dispersion performance and conductivity, the $GNS_1/PSS_{0.5}$ sample was chosen for subsequent use. To verify the excellent dispersion performance of PSS for graphene, we compared the dynamic instability and conductivity of GNS/PSS and GNS/SDBS dispersions. Compared with GNS/SDBS, GNS/PSS dispersion showed better dispersion performance. This excellent dispersion effectively prevents the agglomeration of graphene, thereby benefiting improved conductivity (Fig. S8).

The X-Ray Diffraction (XRD) patterns further confirmed the successful exfoliation results of EG by PSS. The characteristic diffraction peak of pristine EG appears at 2θ = 26.6°, which is related to the crystal plane spacing of graphite [45]. In com-

parison, the intensity of characteristic diffraction peaks of GNS/PSS was notably reduced compared to the original EG (Fig. 2f), which suggests that the number of stacked layers is substantially reduced. This result also indicates that EG has been successfully exfoliated into few-layer GNS. Fourier Transform Infrared Spectroscopy (FTIR) was further used to verify the existence of functional groups on GNS surface (Fig. 2g). The characteristic peak at 3434 cm^{-1} can be attributed to O–H stretching vibrations, which is caused by the oxidation during the exfoliation process. For GNS/PSS, the characteristic peaks at 1008, 1039, 1128 and 1184 cm^{-1} can be attributed to the symmetric and asymmetric stretching vibrations of S–O bonds. In addition, the characteristic peaks at 1415 and 1635 cm^{-1} correspond to the main chain vibrations of benzene ring structures, indicating that PSS is successfully adsorbed on GNS surface. In the Raman spectrum of graphene, the D peak (approximately 1350 cm^{-1}) corresponds to a disordered vibration peak, representing structural defects and edges. The G peak (approximately 1582 cm^{-1}) arises from the in-plane vibration of sp^2 carbon atoms, representing the crystallinity of graphite. A lower I_D/I_G ratio indicates fewer structural defects and edges. After EG is successfully stripped by PSS, the I_D/I_G ratio of GNS/PSS is 0.19, which is slightly higher than that of EG (I_D/I_G = 0.14) (Fig. 2h). This is attributed to the non-covalent modification of GNS by PSS that results in the reduction of the sp^2 area in the plane [46]. The thermal stability of EG, PSS, and GNS/PSS was measured by thermogravimetry (Fig. S9a). The residual mass of EG, PSS, and GNS/PSS at 800°C is 97.9%, 53.3%, and 77.5%, respectively. The weight ratio of GNS to PSS in GNS/PSS is close to the actual value (the weight ratio of GNS to PSS is 1:0.5). EG has excellent thermal stability as evidenced by their nearly linear DTG curves (Fig. S9b). The thermal decomposition temperature of GNS/PSS was 562°C, higher than that of PSS (453.5°C), indicating that the π-π interactions between PSS and GNS enhance the thermal stability of GNS/PSS [47]. The GNS/PSS dispersion maintained good dispersion performance even after 120 days, along with stable conductivity (Fig. S10). This demonstrates the excellent durability and environmental suitability of GNS/PSS. Moreover, compared to other conductive materials such as silver nanowires, liquid metal and carbon nanotubes, EG is not only widely available but also cheaper. Thus, the GNS/PSS dispersion holds promise for cost-effective applications.

Depositing conductive dispersions onto flexible substrates is an effective strategy in maintaining high conductivity, which is a crucial factor in the performance of electronic devices. The adhesion performance between conductive materials and poly-

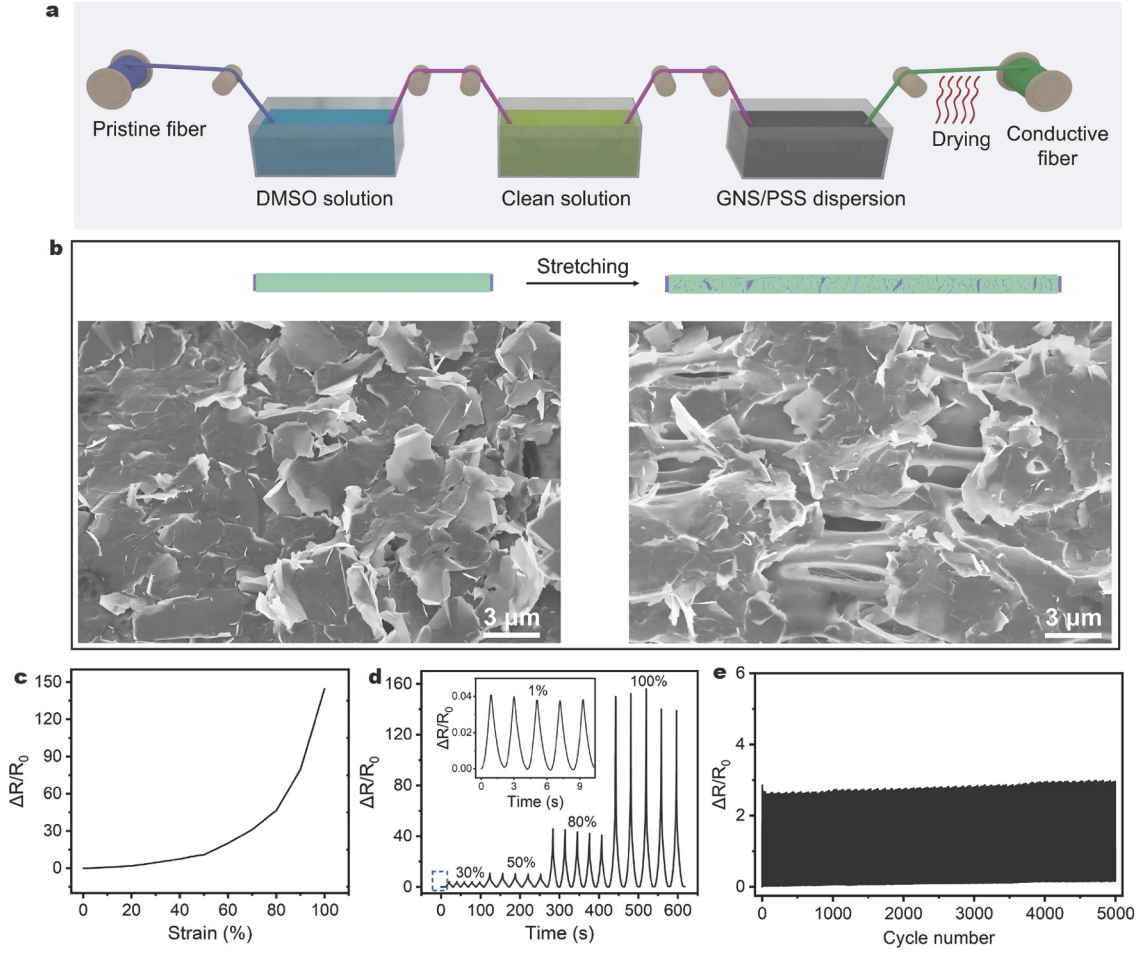

Figure 3 (a) Schematic illustration of the preparation of a GNS/PSS-based stretchable fiber strain sensor. (b) SEM images of a stretchable fiber-strain-sensor surfaces before and after stretching; the applied strain is 50%. (c) The relative resistance change of the stretchable fiber strain sensor under stretching. (d) Repetitive cycles of the fiber strain sensor upon stretching to different strains of 1, 30, 50, 80 and 100; inset shows an enlarged curve of 1% strain. (e) Cycling stability of the fiber strain sensor under a strain of 30%.

mer substrates is crucial for ensuring durability during usage. In our system, the use of PSS significantly enhances adhesion strength with polymer substrates compared to small molecule dispersants like sodium dodecyl benzene sulfonate (Fig. 2i). Consequently, we utilized the GNS/PSS dispersion to fabricate functional conductive fibers/textiles for wearable electronic devices. The fabrication process of conductive fiber is shown in Fig. 3a. The TPU fiber is firstly treated with DMSO to increase the surface roughness, thus facilitating the coating of conductive materials (Fig. S11). A layer of dense GNS/PSS is observed from the cross-section image, indicating that GNS is embedded in the fibers (Fig. S12). On the contrary, some areas on the fiber surface without DMSO pretreatment are not covered with GNS/PSS, resulting in voids, and GNS is not embedded in the fiber from the cross-section image (Fig. S13). The influence of DMSO pretreatment on the adhesion of GNS/PSS conductive layer is explored by applying adhesive tape to the GNS/PSS conductive layer. It can be found the pretreatment with DMSO reduces the detachment of the GNS/PSS conductive layer from fiber substrate (Fig. S14). The resistance of the conductive fiber is optimized with different soaking times. The resistance decreases with increasing soaking time and is almost unchanged after 4 min (Fig. S15).

The GNS/PSS-coated TPU conductive fiber can be used as a stretchable strain sensor to detect mechanical strains. Cracks are observed in the GNS/PSS conductive layer after stretching the fiber due to the different mechanical properties of the conductive materials and stretchable substrate. Fig. 3b shows the GNS/PSS layer in the fiber strain sensor produced microcracks with a strain of 50%, thus increasing the electrical resistance for sensing. The relative change in electrical resistance under strain is shown in Fig. 3c, where the resistance increases with increasing strain. The fiber strain sensor can endure a strain of up to 100% with a gauge factor representing sensitivity of 144.6. The resistance change curves show high repeatability under various strains with a minimum detectable strain as low as 0.1% (Fig. 3d and Fig. S16). Furthermore, the resulting fiber strain sensor shows short response and recovery time of 0.188 s (Fig. S16). The performance under different frequencies is an important index to verify the stability of its fast signal response.

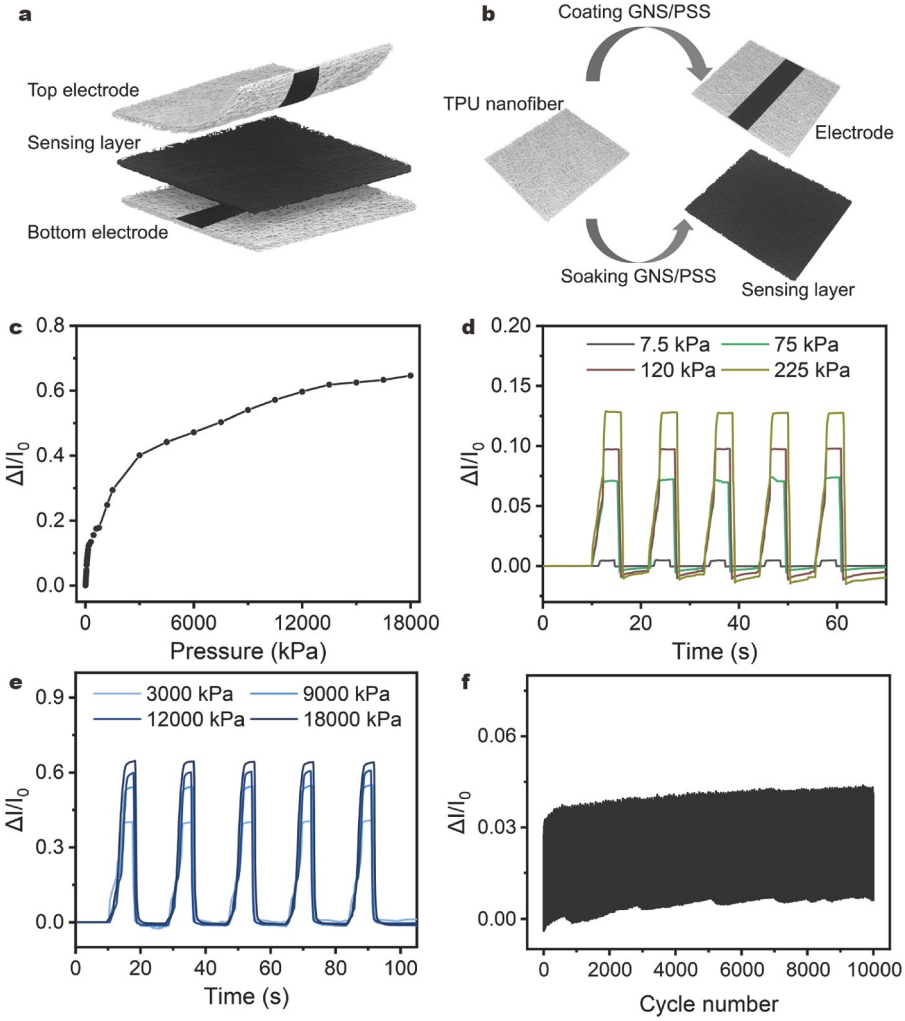

Figure 4 Pressure sensing performance of the pressure sensor based on GNS/PSS-modified nanofiber membrane. (a) Schematic illustration of the structure of the TPU nanofiber membrane-based pressure sensor. (b) Schematic illustration of the preparation of the electrode and the sensing layer. (c) Relative current change of the TPU nanofiber membrane-based pressure sensor under different pressure loadings. Relative current responses of the TPU nanofiber membrane-based pressure sensor under cyclic loading/unloading cycles with (d) low pressures from 7.5 to 225 kPa, and, (e) high pressures from 3000 to 18,000 kPa. (f) Relative current change of the TPU nanofiber membrane-based pressure sensor over 10,000 loading/unloading cycles at a pressure of 10 kPa.

As shown in Fig. S17 the response and recovery curves exhibit symmetry with no significant changes in amplitude from 0.1 to 1 Hz. This indicates that our fiber strain sensor remained stable across different frequency ranges. The fiber strain sensor based on GNS/PSS shows good cyclic durability and can endure a continuous loading-unloading process of 5000 cycles (Fig. 3e).

The fiber-based films typically possess a highly porous structure with interconnected nanoscale pores. Due to their nanoscale/microscale diameters and low density, fiber-based films are lightweight compared to traditional films made of bulk materials. The TPU nanofiber films are fabricated using electrospinning. Their large specific surface areas provide a large number of loading sites for GNS/PSS, making them suitable as flexible and breathable functional materials for pressure sensors. Fig. 4a shows the schematic illustration of the GNS/PSS-TPU nanofiber pressure sensor, which is a typical sandwich structure. The top and bottom electrodes are fabricated by coating GNS/PSS on the surface of the TPU nanofiber membrane, while the middle sensing layer is a fully conductive layer made by soaking GNS/PSS dispersion (Fig. 4b). GNSs are embedded among fiber gaps from the surface and cross-section SEM images (Fig. S18). The work mechanism of our pressure sensor is as following: As the applied external pressure load increases, the sensing layer is compressed so that the spacing between the GNS sheets in the GNS/PSS-TPU composite layer of the intermediate sensing layer gradually decreases until the contacts form conductive paths (Fig. S19). Thus, it can be understood that the pressure-sensitive mechanism is that the number of conductive paths increases due to the applied external pressure loading.

As shown in Fig. 4c, the relative current changes at different pressures are recorded and the device maintains a wide pressure response range by 18,000 kPa. Repeated loading-unloading tests under various pressures proved further the device's stable pressure response and excellent repeatability (Fig. 4d, e). Objects of different weights, such as button battery, stirring magneton and bottle, could be distinguished based on changes in current value (Fig. S20). The nanofiber-based pressure sensor enables a rapid response during pressure loading and unloading processes. The response time and recovery time are 128 and 125 ms, respectively (Fig. S21). The relative current variation of the device over 10,000 cycles of loading-unloading under a pressure of 10 kPa is recorded (Fig. 4f). No significant signal fluctuations are observed, indicating excellent durability and repeatability of the GNS/PSS-based pressure sensor.

Flexible and stretchable wearable devices made of GNS/PSS not only sense mechanical deformations, such as strain and pressure, but also serve as noninvasive electrodes for detecting human-related electrophysiological signals, including ECG and EMG. Real-time monitoring of ECG and EMG signals is of great significance to reflect human health [48–50]. Fig. 5a is a sche-

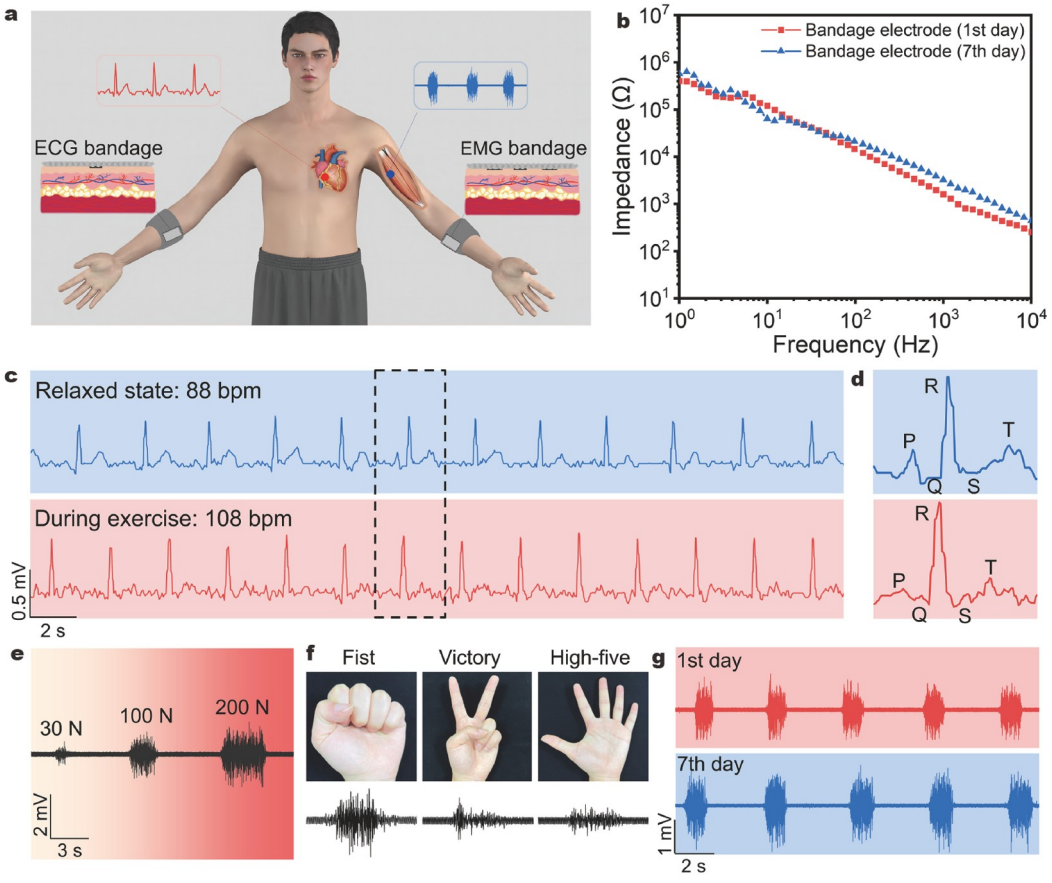

Figure 5 Biopotential signal detection using the fabric bandage electrode. (a) Schematic illustration of the fabric bandage electrode used to measure ECG and EMG signals. (b) Impedance analysis of the fabric bandage electrode on skin on the first and seventh days of use. (c) ECG signals measured with the fabric bandage electrode in relaxed state and during exercise. (d) An enlarged curve of the ECG signals showing a distinguishable rhythm-related PQRST waveform. (e) EMG signals measured under different gripping forces of 30, 100, and 200 N. (f) EMG signals from three hand gestures detected by the bandage electrode. (g) EMG signals measured by the fabric bandage electrodes on the first and seventh days of use.

matic illustration of bandage electrode detecting electrophysiological signals. The TPU nanofiber membrane modified with GNS/PSS dispersion is sewn into the commercial fabric, and the optical images of the bandage electrode for detecting ECG and EMG signals are shown in Fig. S22. The interface impedance between human skin and the bandage electrode shows no significant change after being used 10 times over one week (Fig. 5b). ECG could provide important information for the analysis and diagnosis of arrhythmia and cardiovascular diseases [51,52]. To measure the ECG signals, we placed the fabric bandage electrode on the forearm. As shown in Fig. 5c, ECG signals of the volunteer are reliably recorded before and during exercise, displaying different heart rates of 88 and 108 bpm, respectively. From the enlarged ECG curves, atrial depolarization (P wave), depolarization of ventricles (QRS complex) and ventricle repolarization (T wave) in the PQRST waveforms related to heart rhythm are clearly discernible (Fig. 5d). EMG signal originates from muscle contraction movement reflecting the muscle's activity level [53]. We measured EMG signals at grip forces of 30, 100, and 200 N (Fig. 5e). The resulting EMG signals exhibit increasing amplitudes corresponding to the increased grip strength. This result demonstrates the potential of fabric bandage electrodes for detecting the level of muscle activities. Additionally, different gestures, such as fist, victory, and high-five, could be distinguished from EMG signals (Fig. 5f), which has potential applications in the field of human-computer interaction. Our bandage electrode could easily detect high-quality EMG signals, and furthermore, the signals remain stable even after the bandage electrode is stored for 7 days (Fig. 5g).

In addition to flexible sensing devices, conductive GNS/PSS dispersions can be utilized in fiber-shaped alternating current

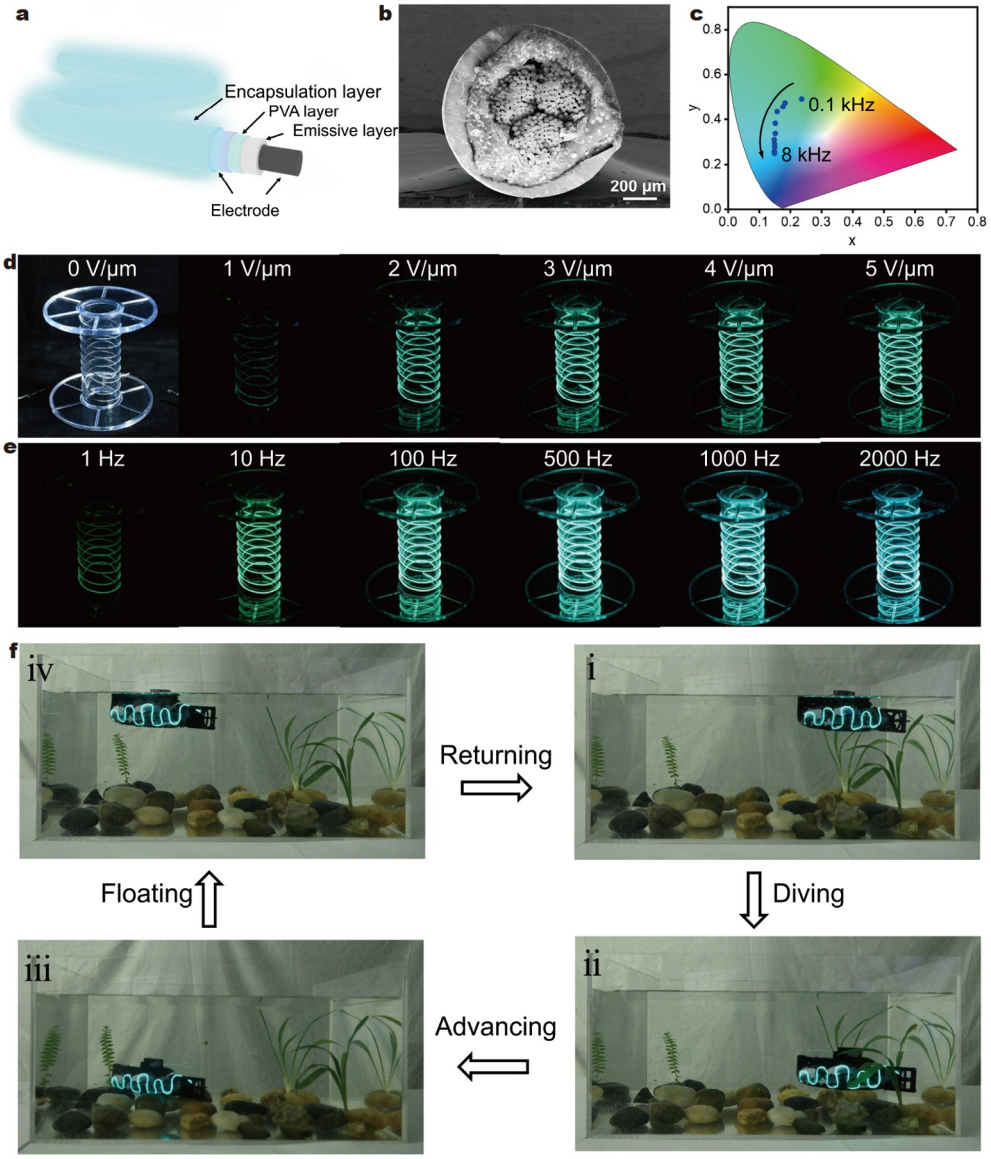

Figure 6 (a) Schematic illustration for the preparation of a coaxial electroluminescent fiber. (b) Cross-sectional SEM image of a coaxial electroluminescent fiber. (c) Dependence of the emission color of coaxial electroluminescent fiber on the frequency increasing from 0.1 to 8 kHz at a fixed voltage of 5 V/μm according to CIE 1931 color space. (d) Photographs of different voltages of coaxial electroluminescent fiber at 100-Hz frequency; (e) Photographs of different frequencies of coaxial electroluminescent fiber at a voltage of 6 V/μm. (f) An electroluminescent fiber is fixed on the submarine model to illuminate the environment during the submarine's (i) diving, (ii) advancing, (iii) floating and (iv) returning.

electroluminescent devices. Commercial PA6 yarn serves as the fiber substrate, which is soaked in GNS/PSS dispersion to produce conductive fiber (Fig. S23). Subsequently, the conductive fiber is successively coated with ZnS:Cu/SBS luminescent material, PVA hydrophilic layer, and an outer electrode of PEDOT:PSS, before being encapsulated with PDMS. The structure of coaxial electroluminescent fiber is shown in Fig. 6a, b. Each layer is well loaded without obvious defects from SEM images (Fig. S24). As mentioned above, the conductivity of GNS/PSS sample decreases with an increase in PSS content. This variation in conductivity could affect the performance of the luminescent devices. For instance, the luminescent intensity of the coaxial electroluminescent fiber decreases as the PSS content increases (Fig. S25). The subsequent luminescent devices are all based on the $GNS_1/PSS_{0.5}$ dispersion. The applied frequency and voltage have a positive effect on the luminance, and a luminance of 50.08 cd/m^2 is obtained at a frequency of 5 kHz and a voltage density of 5.65 V/μm, satisfying the requirements for environmental conditions in darkness (Fig. S26). Fig. 6d depicts the variation in brightness with voltage under a fixed applied frequency. When the voltage is 1 V/μm, the brightness is relatively weak, while it becomes more noticeable when the voltage reaches or exceeds 2 V/μm. In addition, the brightness varies with frequency as shown in the Fig. 6e and Movie S1. The Commission Internationale d'Eclairage (CIE) coordinates of the coaxial electroluminescent fibers are shown in Fig. 6c and Fig. S27. The color coordinate shifts from (0.2362, 0.4417) to (0.1499, 0.2004), and the blue shift phenomenon is obvious in Fig. 6c [54,55]. Furthermore, the coaxial electroluminescent fiber works well under extreme mechanical deformation, such as knotting (Fig. S28).

The resulting coaxial electroluminescent fibers exhibit stable and excellent luminescent characteristics, which have great application potential in clothing decoration, special environment lighting, and healthcare [56–60]. In the ocean exploration, underwater detection equipment is an indispensable facility. Providing underwater lighting for such an equipment facilitates smooth exploration. The flexibility of electroluminescent fiber enables it to conform to the irregular surfaces of the equipment. As a demonstration, an electroluminescent fiber is integrated with a submarine model to illuminate the submarine in complex underwater environments, guiding it to perform maneuvers such as diving, advancing, and floating in specified directions. Its stable luminance performance holds promise for expanding the applications of luminescent devices in the marine field (Fig. 6f and Movie S2).

CONCLUSIONS

In summary, we have developed a stable and versatile conductive aqueous dispersion based on graphene and PSS. Morphological and structural characterizations demonstrate that PSS dispersant effectively disperse graphene in aqueous solution through non-covalent interactions and electrostatic repulsion. The conductive GNS/PSS dispersion can seamlessly integrate with polymer fibers to realize multifunctional conductive fibers. We have fabricated fiber-based flexible mechanical sensors using GNS/PSS-modified fibers and fibrous membranes, including stretchable strain sensors and pressure sensors, capable of a sensing strain as small as 0.1%. Furthermore, electrophysiological electrodes based on GNS/PSS-modified fibrous membranes can accurately detect electrophysiological signals for a long-time, including EMG and ECG. As a proof of concept, a highly flexible GNS/PSS-based coaxial electroluminescent fiber is designed, which can provide illumination for a submarine model to perform complete complex tasks. Given its facile preparation, high conductivity, and versatile applications, the proposed GNS/PSS aqueous dispersion holds significant potential for use in eco-friendly and multifunctional wearable electronic devices.

Received 20 March 2024; accepted 29 April 2024; published online 16 May 2024

1 Ding T, Chan KH, Zhou Y, *et al.* Scalable thermoelectric fibers for multifunctional textile-electronics. Nat Commun, 2020, 11: 6006
2 Yang Q, Xu Z, Fang B, *et al.* MXene/graphene hybrid fibers for high performance flexible supercapacitors. J Mater Chem A, 2017, 5: 22113–22119
3 Liu Y, Tang Y, Guo X, *et al.* Template-free and stretchable conductive fiber with a built-in helical structure for strain-insensitive signal transmission. ACS Appl Mater Interfaces, 2023, 15: 46379–46387
4 Chen M, Wang Z, Zhang Q, *et al.* Self-powered multifunctional sensing based on super-elastic fibers by soluble-core thermal drawing. Nat Commun, 2021, 12: 1416
5 Zhao X, Zhou Y, Xu J, *et al.* Soft fibers with magnetoelasticity for wearable electronics. Nat Commun, 2021, 12: 6755
6 Pan S, Zhu M. Fiber electronics bring a new generation of acoustic fabrics. Adv Fiber Mater, 2022, 4: 321–323
7 Chen C, Feng J, Li J, *et al.* Functional fiber materials to smart fiber devices. Chem Rev, 2023, 123: 613–662
8 Shi X, Zuo Y, Zhai P, *et al.* Large-area display textiles integrated with functional systems. Nature, 2021, 591: 240–245
9 Su Y, Li W, Cheng X, *et al.* High-performance piezoelectric composites *via* β phase programming. Nat Commun, 2022, 13: 4867
10 Pan H, Chen G, Chen Y, *et al.* Biodegradable cotton fiber-based piezoresistive textiles for wearable biomonitoring. Biosens Bioelectron, 2023, 222: 114999
11 Dai J, Xie G, Chen C, *et al.* Hierarchical piezoelectric composite film for self-powered moisture detection and wearable biomonitoring. Appl Phys Lett, 2024, 124: 053701
12 Chen C, Xie G, Dai J, *et al.* Integrated core-shell structured smart textiles for active NO_2 concentration and pressure monitoring. Nano Energy, 2023, 116: 108788
13 Zhang Q, Xie G, Duan M, *et al.* Zinc oxide nanorods for light-activated gas sensing and photocatalytic applications. ACS Appl Nano Mater, 2023, 6: 17445–17456
14 Li Y, Li W, Jin Z, *et al.* Ternary ordered assembled piezoelectric composite for self-powered ammonia detection. Nano Energy, 2024, 122: 109291
15 Lee S, Shin S, Lee S, *et al.* Ag nanowire reinforced highly stretchable conductive fibers for wearable electronics. Adv Funct Mater, 2015, 25: 3114–3121
16 Xiang C, Lu W, Zhu Y, *et al.* Carbon nanotube and graphene nanoribbon-coated conductive kevlar fibers. ACS Appl Mater Interfaces, 2012, 4: 131–136
17 Liang X, Li H, Dou J, *et al.* Stable and biocompatible carbon nanotube ink mediated by silk protein for printed electronics. Adv Mater, 2020, 32: 2000165
18 Chen H, Xu H, Luo M, *et al.* Highly conductive, ultrastrong, and flexible wet-spun PEDOT:PSS/Ionic liquid fibers for wearable electronics. ACS Appl Mater Interfaces, 2023, 15: 20346–20357
19 Zhong J, Chen R, Shan T, *et al.* Continuous fabrication of core-sheath fiber for strain sensing and self-powered application. Nano Energy, 2023, 118: 108950
20 Liang X, Zhu M, Li H, *et al.* Hydrophilic, breathable, and washable graphene decorated textile assisted by silk sericin for integrated multimodal smart wearables. Adv Funct Mater, 2022, 32: 2200162
21 Cao C, Lin Z, Liu X, *et al.* Strong reduced graphene oxide coated *Bombyx mori* silk. Adv Funct Mater, 2021, 31: 2102923
22 Wei Y, Li X, Wang Y, *et al.* Graphene-based multifunctional textile for

sensing and actuating. ACS Nano, 2021, 15: 17738–17747
23 Li P, Yang M, Liu Y, *et al.* Continuous crystalline graphene papers with gigapascal strength by intercalation modulated plasticization. Nat Commun, 2020, 11: 2645
24 Chu Z, Jiao W, Huang Y, *et al.* Superhydrophobic gradient wrinkle strain sensor with ultra-high sensitivity and broad strain range for motion monitoring. J Mater Chem A, 2021, 9: 9634–9643
25 Qiao Y, Jian J, Tang H, *et al.* An intelligent nanomesh-reinforced graphene pressure sensor with an ultra large linear range. J Mater Chem A, 2022, 10: 4858–4869
26 Chang D, Liu J, Fang B, *et al.* Reversible fusion and fission of graphene oxide-based fibers. Science, 2021, 372: 614–617
27 Zelenák F, Kováčová M, Moravec Z, *et al.* Fast, scalable, and environmentally friendly method for production of stand-alone ultrathin reduced graphene oxide paper. Carbon, 2023, 215: 118436
28 Liu Z, Ma Z, Qian B, *et al.* A facile and scalable method of fabrication of large-area ultrathin graphene oxide nanofiltration membrane. ACS Nano, 2021, 15: 15294–15305
29 Cao CF, Yu B, Huang J, *et al.* Biomimetic, mechanically strong supramolecular nanosystem enabling solvent resistance, reliable fire protection and ultralong fire warning. ACS Nano, 2022, 16: 20865–20876
30 Tang P, Deng Z, Zhang Y, *et al.* Tough, strong, and conductive graphene fibers by optimizing surface chemistry of graphene oxide precursor. Adv Funct Mater, 2022, 32: 2112156
31 Zhang Z, Tang L, Chen C, *et al.* Liquid metal-created macroporous composite hydrogels with self-healing ability and multiple sensations as artificial flexible sensors. J Mater Chem A, 2021, 9: 875–883
32 De S, King PJ, Lotya M, *et al.* Flexible, transparent, conducting films of randomly stacked graphene from surfactant-stabilized, oxide-free graphene dispersions. Small, 2010, 6: 458–464
33 Lotya M, Hernandez Y, King PJ, *et al.* Liquid phase production of graphene by exfoliation of graphite in surfactant/water solutions. J Am Chem Soc, 2009, 131: 3611–3620
34 Kumar P, Bohidar HB. Aqueous dispersion stability of multi-carbon nanoparticles in anionic, cationic, neutral, bile salt and pulmonary surfactant solutions. Colloids Surfs A-Physicochem Eng Aspects, 2010, 361: 13–24
35 Vinayan BP, Nagar R, Raman V, *et al.* Synthesis of graphene-multiwalled carbon nanotubes hybrid nanostructure by strengthened electrostatic interaction and its lithium ion battery application. J Mater Chem, 2012, 22: 9949–9956
36 Liu S, Tian J, Wang L, *et al.* Stable aqueous dispersion of graphene nanosheets: noncovalent functionalization by a polymeric reducing agent and their subsequent decoration with Ag nanoparticles for enzymeless hydrogen peroxide detection. Macromolecules, 2010, 43: 10078–10083
37 Coleman JN. Liquid exfoliation of defect-free graphene. Acc Chem Res, 2013, 46: 14–22
38 Ciesielski A, Samorì P. Graphene *via* sonication assisted liquid-phase exfoliation. Chem Soc Rev, 2014, 43: 381–398
39 Marom N, Bernstein J, Garel J, *et al.* Stacking and registry effects in layered materials: The case of hexagonal boron nitride. Phys Rev Lett, 2010, 105: 046801
40 Ardyani T, Mohamed A, Abu Bakar S, *et al.* A guide to designing graphene-philic surfactants. J Colloid Interface Sci, 2022, 620: 346–355
41 Chen Z, Wang J, Pan D, *et al.* Mimicking a dog's nose: Scrolling graphene nanosheets. ACS Nano, 2018, 12: 2521–2530
42 Zhao Z, Cai W, Xu Z, *et al.* Multi-role p-styrene sulfonate assisted electrochemical preparation of functionalized graphene nanosheets for improving fire safety and mechanical property of polystyrene composites. Compos Part B-Eng, 2020, 181: 107544
43 Luo J, Sun C, Chang B, *et al.* MXene-enabled self-adaptive hydrogel interface for active electroencephalogram interactions. ACS Nano, 2022, 16: 19373–19384
44 Eltoukhy Allam N, Nabeel Anwar M, Kuznetsov PV, *et al.* Enzyme-assisted dewatering of oil sands tailings: Significance of water chemistry and biological activity. Chem Eng J, 2022, 437: 135162
45 Abdelkader AM, Kinloch IA, Dryfe RAW. Continuous electrochemical exfoliation of micrometer-sized graphene using synergistic ion intercalations and organic solvents. ACS Appl Mater Interfaces, 2014, 6: 1632–1639
46 Balamurugan T, Berchmans S. Non-enzymatic detection of bilirubin based on a grapheme-polystyrene sulfonate composite. RSC Adv, 2015, 5: 50470–50477
47 He Y, Lin X, Feng Y, *et al.* Carbon nanotube ink dispersed by chitin nanocrystals for thermoelectric converter for self-powering multifunctional wearable electronics. Adv Sci, 2022, 9: 2204675
48 Pan S, Zhang F, Cai P, *et al.* Mechanically interlocked hydrogel–elastomer hybrids for on-skin electronics. Adv Funct Mater, 2020, 30: 1909540
49 He K, Liu Z, Wan C, *et al.* An on-skin electrode with anti-epidermal-surface-lipid function based on a zwitterionic polymer brush. Adv Mater, 2020, 32: 2001130
50 Jin H, Matsuhisa N, Lee S, *et al.* Enhancing the performance of stretchable conductors for e-textiles by controlled ink permeation. Adv Mater, 2017, 29: 1605848
51 Acharya UR, Oh SL, Hagiwara Y, *et al.* A deep convolutional neural network model to classify heartbeats. Comput Biol Med, 2017, 89: 389–396
52 Uchaipichat N, Thanawattano C, Buakhamsri A. The development of ST-episode detection in holter monitoring for myocardial ischemia. Procedia Comput Sci, 2016, 86: 188–191
53 Imai A, Kaneoka K, Okubo Y, *et al.* Trunk muscle activity during lumbar stabilization exercises on both a stable and unstable surface. J Orthop Sports Phys Ther, 2010, 40: 369–375
54 Moon Jeong S, Song S, Lee SK, *et al.* Mechanically driven light-generator with high durability. Appl Phys Lett, 2013, 102: 051110
55 Brubaker CD, Newcome KN, Jennings GK, *et al.* 3D-Printed alternating current electroluminescent devices. J Mater Chem C, 2019, 7: 5573–5578
56 Zhou Y, Cao S, Wang J, *et al.* Bright stretchable electroluminescent devices based on silver nanowire electrodes and high-k thermoplastic elastomers. ACS Appl Mater Interfaces, 2018, 10: 44760–44767
57 Wang J, Yan C, Cai G, *et al.* Extremely stretchable electroluminescent devices with ionic conductors. Adv Mater, 2016, 28: 4490–4496
58 Zhang Z, Cui L, Shi X, *et al.* Textile display for electronic and brain-interfaced communications. Adv Mater, 2018, 30: 1800323
59 Qu C, Zhang Y, Chen Z, *et al.* A flexible and wearable visual pressure sensing system based on piezoresistive sensors and alternating current electroluminescence devices. Adv Mater Technologies, 2024, 9: 2301280
60 Tan YJ, Godaba H, Chen G, *et al.* A transparent, self-healing and high-κ dielectric for low-field-emission stretchable optoelectronics. Nat Mater, 2020, 19: 182–188

Acknowledgements This work was supported by the National Natural Science Foundation of China (52373201, 52103252 and 52090033), the Fundamental Research Funds for the Central Universities (2232024Y-01), and the State Key Laboratory for Modification of Chemical Fibers and Polymer Materials (Donghua University).

Author contributions Pan S and Zhu M conceived and designed the research project. Miao Z performed the experiments and collected the data. Miao Z and Pan S wrote the manuscript. Yu R, Bai X, Du X, Yang Z and Zhou T assisted with some experimental measurements and manuscript correction. All authors contributed to the general discussion.

Conflict of interest The authors declare that they have no conflict of interest.

Supplementary information Experimental details and supporting data are available in the online version of the paper.

Shaowu Pan is currently a professor at the School of Materials Science and Engineering at Donghua University. He received his BE degree in chemistry at Hunan University of Science and Technology in 2009, his MS degree in organic chemistry at South China Normal University in 2012, and his PhD in materials science and engineering at Tongji University in 2015 with a joint study experience at Fudan University. He then worked as a postdoctoral fellow at the School of Materials Science and Engineering, Nanyang Technological University in Singapore before joining Donghua University in 2020. His research interests include smart materials, flexible sensing, and fiber electronics.

用于纤维基可穿戴传感器和电致发光器件的多功能石墨烯/聚电解质水性分散液

缪振宇, 余柔会, 白晓文, 杜相恒, 杨中华, 周涛, 朱美芳, 潘绍武*

摘要 导电分散液是构建用于可穿戴传感器、能源和柔性显示器件中导电纤维/织物的关键组成部分. 尽管石墨烯具有稳定的化学性质和高电导性, 但制备与纤维/织物材料兼容的石墨烯分散液仍然具有挑战性. 本研究通过引入聚苯乙烯磺酸钠(PSS)分散剂, 成功制备了环境友好且稳定的石墨烯水性分散液. PSS通过非共价作用改性石墨烯, 使其表面带负电荷, 由此产生的静电排斥促进了石墨烯的稳定分散. 此外, PSS还有助于石墨烯与基底之间形成牢固的粘附. 我们制备了基于石墨烯改性的纤维和纤维膜的柔性机械传感器, 包括可拉伸应变传感器和压力传感器; 其中, 应变传感器具有100%的高拉伸性和144.6的灵敏度, 也能够感知0.1%的小应变. 此外, 制备的柔性生理电极能够长时间记录肌电信号和心电信号. 作为概念验证, 制备的同轴电致发光纤维能够为潜艇模型提供照明, 以完成水下复杂任务. 这项工作将进一步推动先进纳米材料在可穿戴领域的应用.